

# Structured Unitary Tensor Network Representations for Circuit-Efficient Quantum Data Encoding

Guang Lin<sup>1,2</sup> Toshihisa Tanaka<sup>2,1</sup> Qibin Zhao<sup>\*1,2</sup>

## Abstract

Encoding classical data into quantum states is a central bottleneck in quantum machine learning: many widely used encodings are circuit-inefficient, requiring deep circuits and substantial quantum resources, which limits scalability on quantum hardware. In this work, we propose TNQE, a circuit-efficient quantum data encoding framework built on structured unitary tensor network (TN) representations. TNQE first represents each classical input via a TN decomposition and then compiles the resulting tensor cores into an encoding circuit through two complementary core-to-circuit strategies. To make this compilation trainable while respecting the unitary nature of quantum operations, we introduce a unitary-aware constraint that parameterizes TN cores as learnable block unitaries, enabling them to be directly optimized and directly encoded as quantum operators. The proposed TNQE framework enables explicit control over circuit depth and qubit resources, allowing the construction of shallow, resource-efficient circuits. Across a range of benchmarks, TNQE achieves encoding circuits as shallow as  $0.04 \times$  the depth of amplitude encoding, while naturally scaling to high-resolution images ( $256 \times 256$ ) and demonstrating practical feasibility on real quantum hardware.

## 1. Introduction

In recent years, quantum computing has rapidly advanced from early prototypes with only a few qubits to modern quantum processors with hundreds of qubits (Ladd et al., 2010; Gambetta, 2023). By exploiting quantum mechanical phenomena such as superposition and entanglement, quantum computers enable information representations and computational paradigms that differ fundamentally from

<sup>1</sup>RIKEN Center for Advanced Intelligence Project <sup>2</sup>Tokyo University of Agriculture and Technology. Qibin Zhao, Guang Lin <qibin.zhao@riken.jp, guang.lin@riken.jp>.

Preprint. February 19, 2026.

classical systems (Friedman et al., 2000; Horodecki et al., 2009). These properties suggest the potential for advantages in specific tasks, including the compact representation of high-dimensional data using relatively few qubits (Devadas & Sowmya, 2025). Motivated by this potential, quantum machine learning (QML) has emerged as an interdisciplinary field that seeks to integrate quantum computing with machine learning in order to extend classical learning capabilities (Rodríguez-Díaz et al., 2025; Corli et al., 2025).

Despite rapid progress, QML remains at an early stage of development, with many fundamental challenges still unresolved (Brunet et al., 2024). Among these challenges, the efficient encoding of classical data into quantum systems stands out as a central and pervasive bottleneck (Bermejo et al., 2024). As the entry point from classical information to quantum states, quantum data encoding determines the initial quantum state and the structure of the resulting quantum circuit, thereby shaping all subsequent operations. Consequently, the choice of encoding strategy has a direct impact on key practical factors (Munikote, 2024). Existing quantum data encoding strategies (Weigold et al., 2020; Placidi et al., 2023) often rely on complex and deep circuits to represent classical data, leading to substantial resource overhead and error accumulation (Bose & Verma, 2025). These limitations severely constrain the scalability and applicability of quantum machine learning.

To address these challenges, we propose TNQE, a tensor network (TN)-based framework for circuit-efficient quantum data encoding that constructs executable quantum circuits from structured tensor representations of classical data. TNs provide compact factorizations of high-dimensional arrays into collections of low-rank tensor cores (Kolda & Bader, 2009; Cichocki et al., 2015), offering an explicit handle to trade off representation fidelity and model complexity. Crucially, TNs are also deeply connected to quantum systems, as they can describe quantum states and local operations (Orús, 2014). These properties make TNs a natural intermediate language for encoding classical data to quantum circuits in a structured and efficient manner.

Building on this perspective, TNQE decouples encoding into (i) a TN decomposition of the classical data and (ii) a core-to-circuit conversion step that turns tensor cores into unitaries.

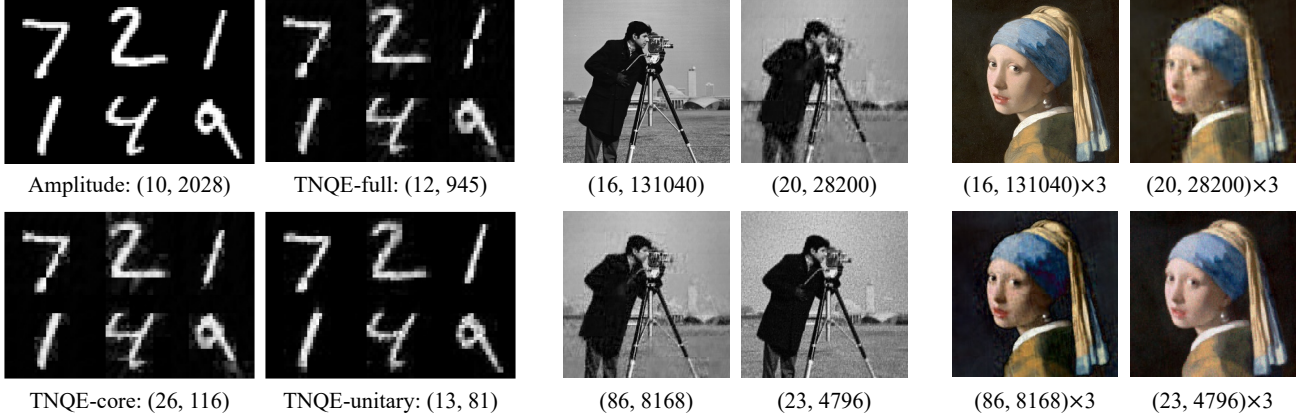


Figure 1. Different-resolution visual comparisons in simulation are conducted using  $32 \times 32$ ,  $256 \times 256$ , and  $256 \times 256 \times 3$  images. The ordering of methods is consistent across resolutions, and the circuit structure is reported as (qubit, depth). Amplitude encoding enables accurate encoding in simulation at the cost of deep circuits, TNQEs provide different trade-offs between qubit and depth.

We instantiate two complementary conversion strategies, including TNQE-full that converts right-canonical MPS cores into isometries and then completes them into local unitaries, yielding a sequential circuit realization; and TNQE-core that prepares each tensor core using a dedicated sub-circuit, avoiding inter-core entangling operations and enabling a shallow, modular, and parallelizable encoding. In addition, we introduce TNQE-unitary, which incorporates a unitary-aware optimization constraint: tensor cores are parameterized directly as learnable block unitaries, so they can be directly optimized and directly encoded as quantum operators without post hoc unitary conversion or synthesis.

We benchmark TNQE across circuit depth, qubit count, operation count, and encoding fidelity (image approximation quality). Across our evaluated settings, TNQE preserves informative structure with substantially shallower circuits, achieving depths as low as  $0.04 \times$  that of amplitude encoding. Notably, while many existing approaches for high-resolution images remain largely theoretical (Lisichenko & Protasov, 2023; Brunet et al., 2024), TNQE successfully encodes  $256 \times 256$  images into quantum circuits in simulation (Figure 1). We further validate practical feasibility by running the resulting circuits on real quantum hardware provided by the IBM Quantum platform<sup>1</sup>. Together, these results demonstrate that TNQE offers a scalable and practical framework for circuit-efficient quantum data encoding.

In summary, our main contributions are as follows:

- We propose TNQE, a TN-based quantum data encoding that bridges classical data and executable quantum circuits via structured core-to-circuit conversion.
- We develop three instantiations, including TNQE-full and TNQE-core as complementary sequential/parallel realizations, and TNQE-unitary with a unitary-aware

constraint that parameterizes cores as learnable block unitaries for direct optimization and execution.

- We demonstrate the scalability and practicality of TNQE through extensive experiments, showing substantial depth reductions (down to  $0.04 \times$  vs. amplitude encoding), successful encoding of high-resolution images, and feasibility on real quantum hardware.

## 2. Related works

**Tensor networks** provide an efficient framework for modeling and processing high-dimensional data through compact structured representations (Kolda & Bader, 2009; Cichocki et al., 2015). Common tensor network formats include matrix product state (MPS, Dilip et al., 2022) and tensor train (TT, Oseledets, 2011), as well as specific structures inspired by quantum, such as quantized tensor train (QTT, Khoromskij, 2011). Notably, these TNs have been widely used in various applications, including both quantum systems (Orús, 2019; Berezutskii et al., 2025) and classical machine learning (Sengupta et al., 2022; Shin et al., 2024). Therefore, TNs provide a potential bridge between classical data and quantum systems, inspiring our TNQE framework for quantum data encoding.

**Quantum data encoding** is a fundamental step in quantum machine learning that encodes classical data into quantum states (Schuld et al., 2014). Early quantum data encoding strategies, including basis encoding and amplitude encoding (Schuld & Killoran, 2019), originate from quantum information processing and quantum algorithm design. However, these encodings often lead to complex circuits that are challenging to implement for image data. Recent works have

<sup>1</sup><https://quantum.cloud.ibm.com>

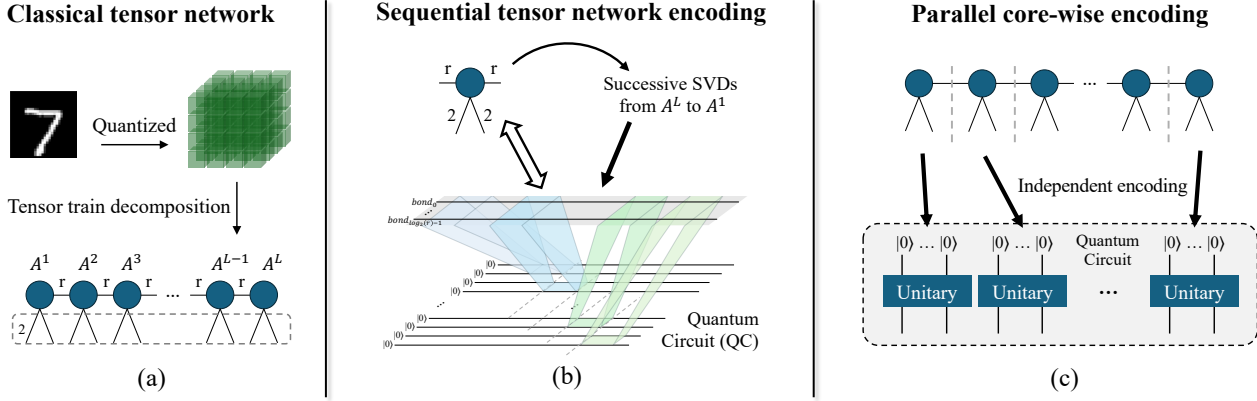


Figure 2. Illustration of the proposed TNQEs. First, a) classical data is represented using quantized tensor train decomposition. Then, b) full tensor network encoding and c) core-wise encoding are developed to convert the core tensors into quantum circuits.

proposed more practical encoding methods for QML. [Dilip et al. \(2022\)](#); [Jobst et al. \(2024\)](#) construct sequential circuits using 1-D MPS and reduce complexity by partitioning images into  $p$ -patches. However, this strategy disrupts spatial structure and rapidly increases complexity as resolution grows. [Ranga et al. \(2024\)](#); [Lu & Shi \(2025\)](#) use CNNs to extract low-dimensional feature  $d$ -vectors in the classical system, and then encode these vectors into quantum circuits. While supporting arbitrary image resolutions, these quantum-classical hybrid methods operate on extracted features instead of raw data, limiting end-to-end (E2E) quantum machine learning as discussed in Section E.

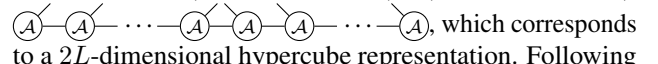
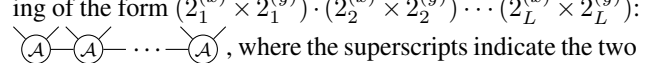
Table 1. Comparison of quantum data encoding methods in terms of scalability and resource requirements. Here  $s^2$  denotes the image size ( $s \times s$ ), and  $r$  and  $N_\ell$  are hyperparameters of TNQE.

Methods	Qubits	Depth	Image size	E2E
Basis encoding	$O(s^2)$	$O(1)$	limited	✓
Amplitude encoding	$O(\log s^2)$	$O(s^2)$	limited	✓
MPS-based encoding	$O(p(\log s^2/p))$	$O(s^2/p)$	limited	✓
CNN-based hybrid	$O(d)$	$O(1)$	arbitrary	✗
TNQE-full	$O(\log s^2 + \log r)$	$O(4r^2 \log s)$	limited	✓
TNQE-core	$O(\log s \log r)$	$O(4r^2)$	scalable	✓
TNQE-unitary	$O(\log s^2 + \log r)$	$O(N_\ell \log s)$	scalable	✓

As summarized in Table 1, conventional methods are constrained by quantum resources and are therefore limited to low-resolution images. While hybrid methods can handle higher-resolution images, the quantum output must still be processed by a CNN to reconstruct the original image, largely undermining the advantages of the quantum system. In contrast, by leveraging TN representations, our proposed TNQE offers flexible control over depth and qubit requirements, enabling scalability to higher-resolution images for end-to-end QML. These properties make TNQE a practical and promising solution for quantum data encoding.

### 3. Preliminary

In this work, we adopt quantized tensor train (QTT, [Khoromskij, 2011](#)) representation as the underlying tensor network structure. QTT is particularly well suited for image data and quantum data encoding, as it exploits spatial structure through mode quantization ([Loeschke et al., 2024](#)) and produces tensor cores with physical dimensions, which naturally align with qubit-based quantum circuits.

QTT builds upon the idea of mode quantization, where each physical dimension is recursively decomposed into binary factors, typically powers of two. Specifically, consider a two-dimensional image defined on an  $s \times s$  size, where  $s = 2^L$ . Through mode quantization, the spatial dimensions are factorized as  $(2_1 \times 2_2 \times \dots \times 2_L) \times (2_1 \times 2_2 \times \dots \times 2_L)$ : , which corresponds to a  $2L$ -dimensional hypercube representation. Following the QTT construction, the binary factors are reordered and grouped according to their hierarchical levels. In particular, the factors corresponding to the same level across different spatial dimensions are grouped together, yielding an ordering of the form  $(2_1^{(x)} \times 2_1^{(y)}) \cdot (2_2^{(x)} \times 2_2^{(y)}) \dots (2_L^{(x)} \times 2_L^{(y)})$ : , where the superscripts indicate the two spatial dimensions ( $x, y$ ) of the image. From the perspective of quantum data encoding, the QTT format provides a particularly favorable interface, as each tensor core can be naturally encoded to a local unitary acting on two qubits.

### 4. Method

As illustrated in Figure 2, our tensor network-based quantum data encoding (TNQE) framework establishes a novel pipeline for transforming classical data into quantum circuits. The framework operates by decoupling the encoding process into (a) classical tensor network decomposition, and (b&c) two encoding quantum circuit realization pipelines.

Based on these pipelines, we develop three TNQEs. TNQE-full converts tensor cores into unitaries, yielding a sequential circuit. TNQE-core encodes each core independently into a sub-circuit, avoiding inter-core entangling operations. TNQE-unitary follows the same circuit construction as TNQE-full, but directly parameterizes the cores as learnable block unitaries, without requiring additional conversion steps. In the following sections, we describe each in detail.

#### 4.1. Full tensor network encoding

In this strategy, we encode QTT cores to a quantum circuit by viewing a right-canonical MPS (Dilip et al., 2022) as a sequence of isometries that can be completed to unitaries and implemented as quantum operators.

**From QTT cores to an MPS.** First, the QTT representation decomposes the input into a sequence of tensor cores  $\mathcal{A}^{(k)} \in \mathbb{C}^{r_{k-1} \times 2 \times \dots \times r_k}$ ,  $k = 1, \dots, L$ , with boundary conditions  $r_0 = r_L = 1$  and  $r_k = r$  for  $2 \leq k \leq L-1$ . Each core contains two binary physical indices  $i_k, j_k \in \{0, 1\}$ . We merge them into a single four-level physical index  $p_k = 2i_k + j_k$ ,  $p_k \in \{0, 1, 2, 3\}$ , which converts the QTT core into an MPS tensor with physical dimension  $d = 4$ :  $\mathcal{A}^{(k)} \mapsto A^{(k)} \in \mathbb{C}^{r_{k-1} \times d \times r_k}$ .

**Right-canonicalization and isometric condition.** Then, to enable an encoding to quantum operators, we further transform the MPS into a right-canonical form by a sequence of singular value decompositions (SVDs, Golub & Reinsch, 1971) applied from right ( $A^L$ ) to left ( $A^1$ ). Specifically, each MPS tensor  $A^{(k)}$  is reshaped into a matrix by grouping  $(p_k, \alpha_k)$  as  $A^{(k)} \mapsto \mathbf{A}^{(k)} \in \mathbb{C}^{r_{k-1} \times (d r_k)}$ , and perform an SVD factorization while absorbing the non-isometric factor into the neighboring matrix to the left, more details are provided in Section A. After this procedure, the matrices  $\mathbf{A}^{(k)}$  for  $k \geq 2$  satisfy the right-isometric condition

$$\mathbf{A}^{(k)}(\mathbf{A}^{(k)})^\dagger = I_{r_{k-1}}. \quad (1)$$

As a consequence of right-canonicalization, the norm of the global state depends solely on the first matrix  $\mathbf{A}^{(1)}$ . Hence, global normalization  $\|\psi\| = 1$  can be enforced by rescaling  $A^{(1)}$  alone, while keeping  $\mathbf{A}^{(k)}$  for  $k \geq 2$  strictly isometric. Each right-canonical matrix can be interpreted as an isometry  $V^{(k)} \equiv (\mathbf{A}^{(k)})^\dagger \in \mathbb{C}^{m \times n}$ ,  $m = d r_k$ ,  $n = r_{k-1}$ , which satisfies  $(V^{(k)})^\dagger V^{(k)} = I_n$ , as detailed in Section A. This isometry maps the incoming bond space to the joint physical and outgoing bond space in a norm-preserving manner.

**Local unitaries and quantum circuit construction.** However, to realize such isometries on a quantum computer, they must be embedded into unitary operations acting on a fixed Hilbert space. Specifically, given an isometry  $V^{(k)} \in \mathbb{C}^{m \times n}$ , we construct

$$U^{(k)} = [V^{(k)} \quad W^{(k)}] \in \mathbb{C}^{m \times m}, \quad (2)$$

where  $W^{(k)} \in \mathbb{C}^{m \times (m-n)}$  is chosen such that its columns are orthogonal to those of  $V^{(k)}$  and orthonormal themselves, i.e.,  $(V^{(k)})^\dagger W^{(k)} = 0$ ,  $(W^{(k)})^\dagger W^{(k)} = I_{m-n}$ . Then  $U^{(k)}$  has

$$\begin{aligned} (U^{(k)})^\dagger U^{(k)} &= \begin{bmatrix} (V^{(k)})^\dagger \\ (W^{(k)})^\dagger \end{bmatrix} \begin{bmatrix} V^{(k)} & W^{(k)} \end{bmatrix} \\ &= \begin{bmatrix} (V^{(k)})^\dagger V^{(k)} & (V^{(k)})^\dagger W^{(k)} \\ (W^{(k)})^\dagger V^{(k)} & (W^{(k)})^\dagger W^{(k)} \end{bmatrix} = \begin{bmatrix} I_n & 0 \\ 0 & I_{m-n} \end{bmatrix} = I_m, \end{aligned} \quad (3)$$

and likewise  $U^{(k)}(U^{(k)})^\dagger = I_m$ . In practice,  $W^{(k)}$  can be obtained by any orthonormal completion procedure (e.g., Gram–Schmidt process (Golub & Van Loan, 2013) used in our experiments). The completion is not unique and any valid completion suffices for circuit realization.

Finally, the sequential quantum circuit is constructed by applying the local unitaries in order. Each unitary  $U^{(k)}$  acts on  $(N_b + 2)$ -qubits, as detailed in Section B, where  $N_b = \log_2 r$  denotes the number of bond qubits and 2 additional qubits correspond to the physical indices  $i_k, j_k$ . Starting from the initial state  $|0\rangle$ , the full quantum state is prepared by sequentially applying these unitaries, i.e.,  $|\psi\rangle = U^{(L)} \dots U^{(2)} U^{(1)} |0\rangle$ .

#### 4.2. Core-wise encoding

In this strategy, each core tensor is encoded independently into a dedicated subset of qubits, and the resulting all qubits are concatenated to form the final quantum circuit, as illustrated in Figure 2c. Unlike TNQE-full, which aims to prepare a single global entanglement over all cores, this strategy avoids inter-core entangling operations and thus yields a shallow and modular circuit.

**Local encoding of a single core.** Given a QTT core  $\mathcal{A}^{(k)}$ , we flatten it into a vector,  $\mathcal{A}^{(k)} \mapsto \mathbf{v}^{(k)} \in \mathbb{C}^{N_k}$ , where the implementation assumes  $N_k$  is a power of two and  $N_k = 4r_{k-1}r_k$ . We then normalize it to form

$$|\psi_k\rangle = \frac{\mathbf{v}^{(k)}}{\|\mathbf{v}^{(k)}\|_2}, \quad \|\mathbf{v}^{(k)}\|_2 > 0. \quad (4)$$

Each  $|\psi_k\rangle$  is prepared on a dedicated register of  $\log_2(N_k)$  qubits via amplitude encoding (Placidi et al., 2023; Ran & Su, 2023). Nevertheless, we do not impose hard constraints on the ranks during tensor decomposition. Instead, the power-of-two requirement is satisfied by zero padding and setting  $N_k$  to the smallest power of two exceeding  $4r_{k-1}r_k$ .

**Quantum circuit construction.** The full encoded state is obtained by preparing all cores on disjoint qubit registers,

$$|\Psi\rangle = \bigotimes_{k=1}^L |\psi_k\rangle. \quad (5)$$

By construction, the circuit introduces no entangling gates across different registers (sub-circuits). As a result, the sub-circuits can be executed independently and in parallel, and the overall circuit depth is bounded by the maximum depth of the individual sub-circuits, rather than scaling with operations on the full  $2^{2L}$ -dimensional Hilbert space.

### 4.3. Unitary-aware tensor network optimization

While TNQE-full is effective, its post hoc unitary synthesis requires an iterative quantum shannon decomposition (Section B), which still results in excessively deep circuits.

Here, we establish a distinct paradigm in which TNQE-unitary directly optimizes quantum operations and interprets the resulting unitaries as tensor cores. This design ensures that all intermediate representations correspond to executable quantum operators, eliminates the need for unitary completion after optimization, and enables explicit control over circuit complexity through parameterization.

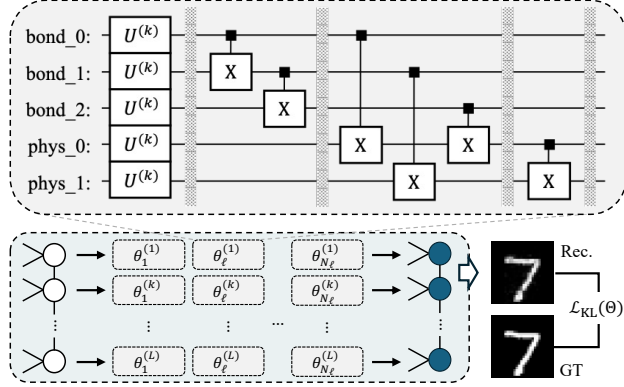


Figure 3. Illustration of TNQE-unitary. Each core is parameterized by a learnable block unitary acting on the bond and physical qubits, with  $N_\ell$  layers of single-qubit rotations and fixed entanglers.

**Parameterized block unitaries.** For each tensor core, we introduce a learnable block unitary  $U^{(k)}(\theta^{(k)})$ ,  $\theta^{(k)} \in \mathbb{R}^{(2 \times (N_b+2) \times N_\ell)}$ , where  $\theta$  denotes all optimized parameters, including 2 rotation operations on  $N_b + 2$  qubits for  $N_\ell$  circuit layers. As detailed in Figure 3, we implement  $U^{(k)}(\theta^{(k)})$  as  $N_\ell$  layers of a) single-qubit rotations and b) fixed entanglers:

a) For layer  $\ell$  and qubit  $q$ , we have

$$U_{1q}(\alpha_{\ell,q}^{(k)}, \beta_{\ell,q}^{(k)}) = R_Z(\beta_{\ell,q}^{(k)}) R_Y(\alpha_{\ell,q}^{(k)}), \quad (6)$$

with (Nielsen & Chuang, 2010)

$$R_Y(\alpha) = e^{-i\alpha Y/2} = \begin{pmatrix} \cos(\alpha/2) & -\sin(\alpha/2) \\ \sin(\alpha/2) & \cos(\alpha/2) \end{pmatrix}, \quad (7)$$

$$R_Z(\beta) = e^{-i\beta Z/2} = \begin{pmatrix} e^{-i\beta/2} & 0 \\ 0 & e^{i\beta/2} \end{pmatrix}.$$

b) Following hardware-efficient designs (Kandala et al., 2017; Huggins et al., 2019), the entangler  $U_e$  is composed of CNOT gates with a fixed pattern including bond-to-bond CNOT $_{q \rightarrow q+1}$ , bond-to-physical CNOT $_{q \rightarrow p(q)}$ , and physical-to-physical CNOT $_{p_0 \rightarrow p_1}$ .

Consequently, the full block unitary is constructed by

$$U^{(k)}(\theta^{(k)}) = \prod_{\ell=1}^{N_L} (U_e U_\ell^{(k)}), U_\ell^{(k)} = \bigotimes_{q=0}^{n-1} U_{1q}(\alpha_{\ell,q}^{(k)}, \beta_{\ell,q}^{(k)}), \quad (8)$$

as illustrated in Figure 3.

**From unitaries to isometric QTT cores.** To recover an isometry compatible with QTT cores, we extract the first  $n$  columns of  $U^{(k)}$ , i.e.,  $V^{(k)} = U^{(k)}(:, 0:n) \in \mathbb{C}^{m \times n}$ . We then reshape  $V^{(k)}$  into the QTT cores  $\mathcal{A}^{(k)}$  by interpreting its row index as a composite of physical outputs  $i_k, j_k$  and bond output  $r_k$ :

$$\mathcal{A}_{r_{k-1}, i_k, j_k, r_k}^{(k)} \equiv \langle r_k, i_k, j_k | V^{(k)} | r_{k-1} \rangle. \quad (9)$$

In this way, the tensor network is defined by a set of quantum operations, and the resulting cores can be directly interpretable as executable quantum circuits.

**Optimization objective.** Let  $X(\Theta)$  denote the reconstructed image obtained by contracting the resulting QTT cores, where  $\Theta = \{\theta^{(k)}\}_{k=1}^L$ . We optimize  $\Theta$  by minimizing the Kullback–Leibler divergence (Kullback & Leibler, 1951) between the normalized target image  $Y$  and the Born probability distribution induced by  $X(\Theta)$ :

$$\mathcal{L}_{\text{KL}}(\Theta) = \sum_{i,j} p_Y(i,j) \left[ \log p_Y(i,j) - \log p_X(i,j; \Theta) \right], \quad (10)$$

where  $p_X(i,j; \Theta) = |X_{ij}(\Theta)|^2 / \sum_{i,j} |X_{ij}(\Theta)|^2$  and  $p_Y(i,j) = Y_{ij} / \sum_{i,j} Y_{ij}$ . After optimization, the learned parameters  $\Theta$  immediately specify the corresponding quantum circuit blocks  $U^{(k)}(\theta^{(k)})$  without additional unitary completion or gate synthesis.

**Remark.** Classical amplitude encoding directly prepares a global quantum state whose amplitudes represent the entire pixel space. While this enables an exponential compression of data into  $2L$  qubits, the corresponding circuits typically involve operations acting across a large number of qubits (Figure 4a), which leads to deep circuits in practice. In contrast, TNQE shifts the encoding object from the full pixel space to local tensor cores. For TNQE-full and TNQE-unitary, each tensor core is mapped to a local unitary acting on a limited qubits, resulting in a structured circuit (Figure 4b). For TNQE-core, tensor cores are encoded independently on disjoint sub-circuits, avoiding long-range entangling operations across different cores and further reducing circuit depth (Figure 4c).

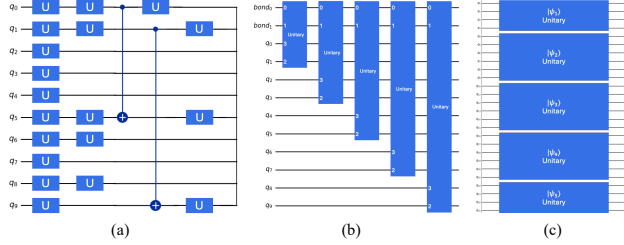


Figure 4. Comparison of quantum circuit for (a) amplitude encoding (partially shown due to its depth), (b) TNQE-full encoding and TNQE-unitary encoding, and (c) TNQE-core encoding.

Overall, by operating on tensor cores rather than directly on the global pixel space, TNQE provides a structured and hardware-compatible strategy to quantum data encoding.

## 5. Experiments

### 5.1. Experimental setup

**Dataset:** We evaluate the proposed TNQE methods on the widely used MNIST dataset (LeCun, 1998), which represents a challenging benchmark for quantum data encoding. MNIST consists of handwritten digits with a resolution of  $28 \times 28$  pixels. To accommodate the power-of-two structure required by our tensor network representation, all images are zero-padded with a padding width of 2, resulting in images of size  $32 \times 32$ . For TNQE-unitary, we experiment on a subset of 1000 images from MNIST to explore the impact of different hyperparameters on performance. For  $256 \times 256$  image, we use two well-known images: the grayscale image Cameraman and the color image Girl with a Pearl Earring.

**Evaluation metrics:** We evaluate the proposed TNQE methods using multiple criteria, including image approximation quality, circuit structure. Image approximation quality is measured using mean squared error (MSE), binary cross entropy (BCE), peak signal-to-noise ratio (PSNR), and structural similarity index measure (SSIM). We further evaluate the semantic information preserved in these images using two classical classifiers.

**Implementation details:** We use Qiskit (Javadi-Abhari et al., 2024) to simulate the quantum circuits generated by the proposed TNQEs. The simulations are performed on a classical computer with sufficient computational resources to handle the quantum circuit simulations.

### 5.2. Results and analysis

#### 5.2.1. QUANTUM CIRCUIT COMPARISON

In this section, we construct quantum circuits for MNIST images and compare the circuit structure of multiple methods, as summarized in Table 2. We set  $r = 4$  for TNQE-full and TNQE-core, and  $r = 8$  with  $N_l = 4$  for TNQE-unitary.

Table 2. Comparison of quantum circuits on  $32 \times 32$  images.

Methods	Qubits	Depth	Unitary	CNOT	Ops.
Baseline (Amplitude)	<b>10</b>	2028	1023	1013	2036
Automatic encoding	<b>10</b>	208	371	129	500
TNQE-full	12	945	900	475	1375
TNQE-core	26	116	219	193	412
TNQE-unitary	13	<b>81</b>	<b>100</b>	<b>120</b>	<b>220</b>

As discussed earlier, basis encoding requires 1024 qubits, making it impractical for current quantum hardware. Amplitude encoding (Schuld & Killoran, 2019) reduces the qubit requirement to 10 by encoding the entire pixel space into a quantum circuit, but at the cost of a deep circuit with a large number of operators. We refer to this method as a key baseline for comparison. Placidi et al. (2023) adopt automatic encoding (Shirakawa et al., 2024) to construct shallower and more efficient circuits for MNIST images; however, this also introduces noticeable approximation errors, as shown in Figure 6. In contrast, TNQEs leverage tensor network representations rather than entire pixels to achieve a more favorable balance between qubit count and circuit depth. The TNQE-full strategy introduces two additional bond qubits, yet results in a  $0.47 \times$  circuit depth compared to the baseline. The TNQE-core strategy further achieves a reduction to only 116 circuit depth ( $0.06 \times$ ) by increasing the qubits to 26. Regarding TNQE-unitary strategy, the circuit depth is controllable and directly determined by setted  $N_\ell$ . We find that a circuit with only 81 circuit depth ( $0.04 \times$ ) is already sufficient to encode MNIST images, which is substantially shallower than that required by all other methods.

In addition, we evaluate the scalability of different quantum data encoding methods as the image size increases from

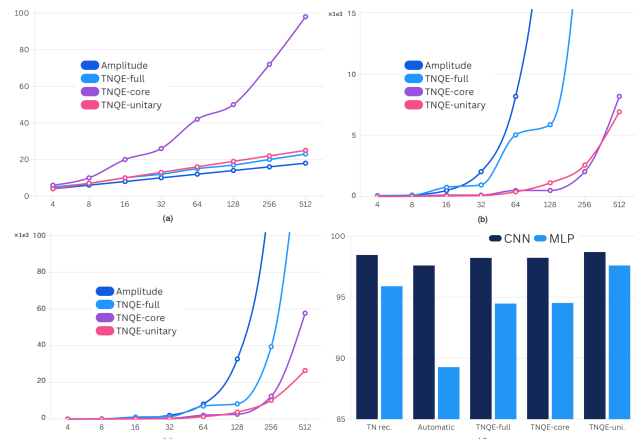


Figure 5. Scalability of different quantum data encoding methods. (a) The number of qubits, (b) circuit depth, and (c) the number of quantum operators as image size increases from  $4 \times 4$  to  $512 \times 512$ . (d) Classification accuracy (%) on approximated MNIST images using CNN and MLP classifiers.

$4 \times 4$  to  $512 \times 512$ , as shown in Figure 5a-c. The amplitude encoding (baseline) exhibits exponential growth in depth and operators, rendering it impractical for larger images. Compared with the baseline, the advantages of our TNQE methods are substantial. Specifically, TNQE-full effectively reduces circuit complexity while maintaining a small number of qubits. In contrast, TNQE-core leverages a larger number of qubits to achieve a more pronounced reduction in circuit complexity. These two strategies exhibit complementary strengths and are suitable for different application scenarios. Finally, TNQE-unitary demonstrates the best scalability, with both qubit count and circuit complexity increasing much more slowly with image size than others. This makes TNQE-unitary particularly promising for encoding high-resolution images in the future.

### 5.2.2. IMAGE APPROXIMATION QUALITY

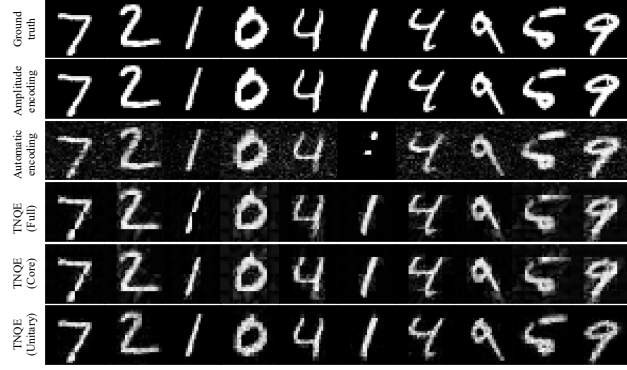


Figure 6. Comparison of MNIST images  $32 \times 32$  from different quantum data encoding methods in simulation.

After discussing the circuit complexity, we further evaluate their performance in terms of image approximation quality, including visual and quantitative comparisons.

**Visual comparisons:** In Figure 6, we present a visual comparison of MNIST images approximated using different quantum data encoding methods in simulation. The first row displays the original images as ground truth and the second row shows the images from amplitude encoding, which serves as a key baseline for comparison. Automatic encoding (Placidi et al., 2023) also encodes the entire pixel space into the amplitudes, which leads to substantial error accumulation and visible artifacts, as shown in the third row. There are pronounced background grain and information loss, which substantially degrade approximation quality.

In contrast, our TNQE strategies encode the tensor network representation rather than operating directly on the entire pixel space. By first factorizing each image into a sequence of tensor cores and then encoding these cores into a quantum circuit, the encoding procedure becomes more local and accurate. Notably, each step acts on a single tensor core and

applies only local operations on a small subset of qubits, instead of performing complex global operations across all qubits. This pipeline significantly reduces circuit complexity and error accumulation, demonstrating that TNQE provides a promising solution for quantum data encoding.

Table 3. Quantitative comparisons of approximated image using quantum data encoding methods in simulation on MNIST dataset.

Methods	MSE	BCE	PSNR	SSIM
<b>Results with original image</b>				
TN reconstruction	0.013135	0.113215	19.3358	0.924981
Automatic encoding	0.015656	0.147523	18.3669	0.882500
TNQE-full	0.015700	0.129583	18.6845	0.906974
TNQE-core	0.015639	0.129311	18.6903	0.907203
TNQE-unitary	<b>0.011249</b>	<b>0.092333</b>	<b>20.5837</b>	<b>0.915903</b>
<b>Results with referenced image</b>				
TN reconstruction	0.013135	0.113215	19.3358	0.924981
Automatic encoding	0.015656	0.147523	18.3669	0.882500
TNQE-full	0.002234	0.165439	28.4850	0.983236
TNQE-core	<b>0.002182</b>	0.165311	<b>28.4913</b>	<b>0.983443</b>
TNQE-unitary	0.011249	<b>0.092333</b>	20.5837	0.915903

**Quantitative comparisons:** We compare different quantum data encoding methods on MNIST using multiple evaluation metrics, including MSE, BCE, PSNR, and SSIM. In addition, we evaluate classification accuracy on approximated images as an indicator of semantic information preservation.

As shown in the top table of Table 3, TNQE-unitary consistently outperforms other methods across all metrics, demonstrating its ability to preserve information with fewer quantum operators. When evaluated with their respective reference images, the other two TNQE methods also show clear advantages. Specifically, original images serve as references for TN, automatic, and TNQE-unitary encodings, while TN-reconstructed images are used for the remaining two TNQE methods. Under this comparison, TNQE-core achieves an MSE of 0.002182, a PSNR of 28.4913, and an SSIM of 0.983443. These results suggest that TNQE’s performance is partially limited by the quality of the tensor cores and that advances in TNs can directly improve TNQE, pointing to a promising direction in the future.

For a more comprehensive evaluation, we conduct classification experiments using CNN and MLP on MNIST, as shown in Figure 5d and Figure 9. The TNQE methods maintain high accuracy, and similarly to the above observations, TNQE-unitary achieves the best accuracy while using fewer quantum operators. This demonstrates that the TNQE methods effectively preserve the semantic information of images, and that directly optimizing the quantum operators is a highly efficient strategy.

### 5.2.3. ABLATION AND REAL QUANTUM EXPERIMENTS

In this section, we conduct ablation studies to analyze the impact of key hyperparameters with 1K MNIST images.

Table 4. Ablation study on different ranks using TNQE on MNIST. The circuit structure is reported as (qubit, depth).

Methods	Rank	1	2	3	4	5	8	9	16
Full	MSE	0.088905	0.056156	0.032136	0.014735	0.008940	0.001833	0.001195	0.003042
	Structure	(10, 7)	(11, 195)	(12, 945)	(12, 945)	(13, 4185)	(13, 4185)	(14, 17625)	(14, 17625)
Core	MSE	0.089138	0.056174	0.032164	0.014731	0.008943	0.001852	0.001185	0.002972
	Structure	(10, 4)	(18, 24)	(26, 116)	(26, 116)	(31, 242)	(34, 496)	(39, 1006)	(42, 2028)
Unitary	MSE	0.162642	0.045030	0.018398	0.018493	0.011287	0.011249	0.008355	0.008307
	Structure	(10, 8)	(11, 56)	(12, 61)	(12, 61)	(13, 81)	(13, 81)	(14, 82)	(14, 82)

As shown in Table 4 and Table 6, we vary the rank of tensor network and evaluate the image approximation quality. Since the bond qubits depend on  $\log_2(r)$ , we conduct experiments covering rank ranges corresponding to 0 to 4 bonds. For the first two TNQE methods, increasing the rank consistently improves performance, as bigger ranks allow for a more expressive tensor network representation; however, this improvement comes at the cost of a substantial increase in circuit depth. In contrast, TNQE-unitary remains largely unaffected by increases in rank, as it is governed by a fixed number of  $N_\ell$ , as shown in Figure 7.

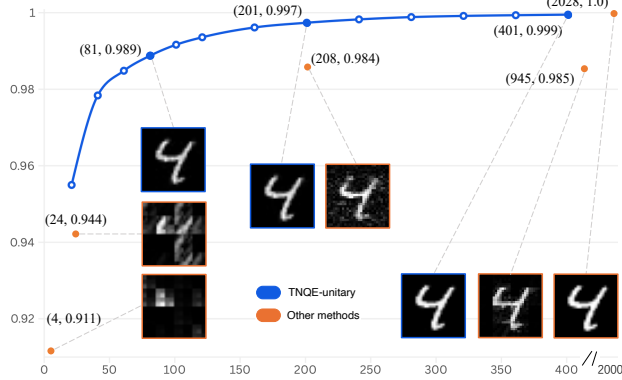


Figure 7. The impact of  $N_\ell$  for TNQE-unitary. To facilitate a comparison with other methods,  $N_\ell$  converts into the corresponding circuit depth on the x-axis and  $1 - \text{MSE}$  on the y-axis. The detailed numerical results are provided in Table 7.

Similarly, increasing  $N_\ell$  enhances the expressiveness of the block-unitary, leading to increased circuit depth and improved image approximation quality. We also present the performance of other methods across different depths. TNQE-unitary achieves strong performance with relatively few depths, highlighting its high encoding efficiency.

**Experiment on real quantum hardware** We further validate our method on real quantum hardware with four different quantum processing units (QPUs) using 100 MNIST images, as shown in Table 5. While deeper and more complex circuits can theoretically provide stronger representational capacity, as exemplified by amplitude encoding in Figure 6, hardware noise on QPUs causes such circuits to

suffer from catastrophic error accumulation, as shown in Figure 8. In contrast, our method preserves semantic information under hardware noise, highlighting the practical potential of TNQE on QPUs. Additional discussions and high-resolution experiments are provided in Section E.

Table 5. Quantitative comparisons on real quantum hardware.

QPUs	Methods	MSE	BCE	PSNR	SSIM
ibm_torino (Heron r1)	Amp.	0.112202	0.488010	9.6688	0.008421
	Auto.	0.050782	0.268235	13.2173	0.554541
	Ours	<b>0.034157</b>	<b>0.193016</b>	<b>15.0322</b>	<b>0.735706</b>
ibm_fez (Heron r2)	Amp.	0.107725	0.666679	9.9193	0.000325
	Auto.	0.053146	0.270768	13.2744	0.567423
	Ours	<b>0.029948</b>	<b>0.183303</b>	<b>15.6425</b>	<b>0.773744</b>
ibm_boston (Heron r3)	Amp.	0.107459	0.568601	9.9130	0.022531
	Auto.	0.041765	0.221006	14.2244	0.627775
	Ours	<b>0.028272</b>	<b>0.174792</b>	<b>15.8837</b>	<b>0.789393</b>

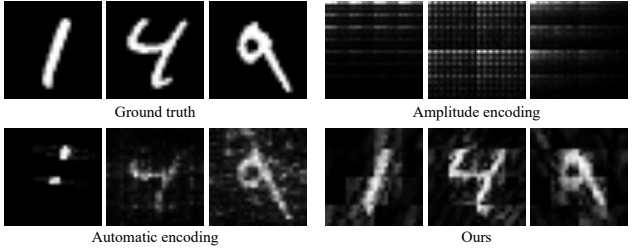


Figure 8. Visual comparisons on ibm\_boston with Heron r3.

## 6. Conclusion

In this work, we propose TNQE, a novel tensor network-based framework for structured and circuit-efficient quantum data encoding. By leveraging the intrinsic connections between tensor networks and quantum systems, we propose three strategies based on tensor network decompositions. Extensive experiments demonstrate that TNQE enables shallow and resource-efficient quantum circuits while preserving informative structure. Moreover, TNQE naturally scales to high-resolution data, and we further validate its practicality on real quantum hardware. Despite these advantages, there remain some open questions and many promising directions to explore related to TNQE, which we discuss in Section E.

## References

Berezutskii, A., Liu, M., Acharya, A., Ellerbrock, R., Gray, J., Haghshenas, R., He, Z., Khan, A., Kuzmin, V., Lyakh, D., et al. Tensor networks for quantum computing. *Nature Reviews Physics*, 7(10):581–593, 2025.

Bermejo, P., Braccia, P., Rudolph, M. S., Holmes, Z., Cincio, L., and Cerezo, M. Quantum convolutional neural networks are (effectively) classically simulable. *arXiv preprint arXiv:2408.12739*, 2024.

Bose, B. and Verma, S. Quantum data encoding and variational algorithms: A framework for hybrid quantum classical machine learning. *arXiv preprint arXiv:2502.11951*, 2025.

Brunet, T., Tolley, E., Corda, S., Ilic, R., Broekema, P. C., and Kneib, J.-P. Quantum radio astronomy: Data encodings and quantum image processing. *Astronomy and Computing*, 47:100796, 2024.

Cichocki, A., Mandic, D., De Lathauwer, L., Zhou, G., Zhao, Q., Caiafa, C., and Phan, H. A. Tensor decompositions for signal processing applications: From two-way to multiway component analysis. *IEEE signal processing magazine*, 32(2):145–163, 2015.

Corli, S., Moro, L., Dragoni, D., Dispenza, M., and Prati, E. Quantum machine learning algorithms for anomaly detection: A review. *Future Generation Computer Systems*, 166:107632, 2025.

Devadas, R. M. and Sowmya, T. Quantum machine learning: A comprehensive review of integrating ai with quantum computing for computational advancements. *MethodsX*, pp. 103318, 2025.

Dilip, R., Liu, Y.-J., Smith, A., and Pollmann, F. Data compression for quantum machine learning. *Physical Review Research*, 4(4):043007, 2022.

Friedman, J. R., Patel, V., Chen, W., Tolpygo, S., and Lukens, J. E. Quantum superposition of distinct macroscopic states. *nature*, 406(6791):43–46, 2000.

Gambetta, J. The hardware and software for the era of quantum utility is here. <https://www.ibm.com/quantum/blog/quantum-roadmap-2033>, 2023.

Golub, G. H. and Reinsch, C. Singular value decomposition and least squares solutions. In *Linear algebra*, pp. 134–151. Springer, 1971.

Golub, G. H. and Van Loan, C. F. *Matrix computations*. JHU press, 2013.

Horodecki, R., Horodecki, P., Horodecki, M., and Horodecki, K. Quantum entanglement. *Reviews of modern physics*, 81(2):865–942, 2009.

Huggins, W., Patil, P., Mitchell, B., Whaley, K. B., and Stoudenmire, E. M. Towards quantum machine learning with tensor networks. *Quantum Science and technology*, 4(2):024001, 2019.

Javadi-Abhari, A., Treinish, M., Krsulich, K., Wood, C. J., Lishman, J., Gacon, J., Martiel, S., Nation, P. D., Bishop, L. S., Cross, A. W., et al. Quantum computing with qiskit. *arXiv preprint arXiv:2405.08810*, 2024.

Jobst, B., Shen, K., Riofrío, C. A., Shishenina, E., and Pollmann, F. Efficient mps representations and quantum circuits from the fourier modes of classical image data. *Quantum*, 8, 2024. ISSN 2521-327X.

Kandala, A., Mezzacapo, A., Temme, K., Takita, M., Brink, M., Chow, J. M., and Gambetta, J. M. Hardware-efficient variational quantum eigensolver for small molecules and quantum magnets. *nature*, 549(7671):242–246, 2017.

Khoromsjij, B. N. O (d log n)-quantics approximation of n-d tensors in high-dimensional numerical modeling. *Constructive Approximation*, 34:257–280, 2011.

Kingma, D. P. Adam: A method for stochastic optimization. *arXiv preprint arXiv:1412.6980*, 2014.

Kolda, T. G. and Bader, B. W. Tensor decompositions and applications. *SIAM review*, 51(3):455–500, 2009.

Krol, A. M. and Al-Ars, Z. Beyond quantum shannon: Circuit construction for general n-qubit gates based on block zxz-decomposition. *arXiv preprint arXiv:2403.13692*, 2024.

Kullback, S. and Leibler, R. A. On information and sufficiency. *The annals of mathematical statistics*, 22(1):79–86, 1951.

Ladd, T. D., Jelezko, F., Laflamme, R., Nakamura, Y., Monroe, C., and O’Brien, J. L. Quantum computers. *nature*, 464(7285):45–53, 2010.

LeCun, Y. The mnist database of handwritten digits. <http://yann.lecun.com/exdb/mnist/>, 1998.

Lisnichenko, M. and Protasov, S. Quantum image representation: A review. *Quantum Machine Intelligence*, 5(1):2, 2023.

Loeschke, S. B., Wang, D., Leth-Espensen, C. M., Belongie, S., Kastoryano, M., and Benaim, S. Coarse-to-fine tensor trains for compact visual representations. In *International Conference on Machine Learning*, pp. 32612–32642. PMLR, 2024.

Lu, Y. and Shi, J. Fidelity-preserving quantum encoding for quantum neural networks. *arXiv preprint arXiv:2511.15363*, 2025.

Munikote, N. Comparing quantum encoding techniques. *arXiv preprint arXiv:2410.09121*, 2024.

Nielsen, M. A. and Chuang, I. L. *Quantum computation and quantum information*. Cambridge university press, 2010.

Orús, R. A practical introduction to tensor networks: Matrix product states and projected entangled pair states. *Annals of physics*, 349:117–158, 2014.

Orús, R. Tensor networks for complex quantum systems. *Nature Reviews Physics*, 1(9):538–550, 2019.

Oseledets, I. V. Tensor-train decomposition. *SIAM Journal on Scientific Computing*, 33(5):2295–2317, 2011.

Placidi, L., Hataya, R., Mori, T., Aoyama, K., Morisaki, H., Mitarai, K., and Fujii, K. Mnisq: A large-scale quantum circuit dataset for machine learning on/for quantum computers in the nisq era. *arXiv preprint arXiv:2306.16627*, 2023.

Ran, S.-J. and Su, G. Tensor networks for interpretable and efficient quantum-inspired machine learning. *Intelligent Computing*, 2:0061, 2023.

Ranga, D., Prajapat, S., Akhtar, Z., Kumar, P., and Vasilakos, A. V. Hybrid quantum-classical neural networks for efficient mnist binary image classification. *Mathematics*, 12(23):1–22, 2024.

Rodríguez-Díaz, F., Gutiérrez-Avilés, D., Troncoso, A., and Martínez-Álvarez, F. A survey of quantum machine learning: Foundations, algorithms, frameworks, data and applications. *ACM Computing Surveys*, 58(4):1–35, 2025.

Schuld, M. and Killoran, N. Quantum machine learning in feature hilbert spaces. *Physical review letters*, 122(4):040504, 2019.

Schuld, M., Sinayskiy, I., and Petruccione, F. The quest for a quantum neural network. *Quantum Information Processing*, 13(11):2567–2586, 2014.

Sengupta, R., Adhikary, S., Oseledets, I., and Biamonte, J. Tensor networks in machine learning. *European Mathematical Society Magazine*, pp. 4–12, 2022.

Shende, V. V., Bullock, S. S., and Markov, I. L. Synthesis of quantum logic circuits. In *Proceedings of the 2005 Asia and South Pacific Design Automation Conference*, pp. 272–275, 2005.

Shin, S., Teo, Y. S., and Jeong, H. Dequantizing quantum machine learning models using tensor networks. *Physical Review Research*, 6(2):023218, 2024.

Shirakawa, T., Ueda, H., and Yunoki, S. Automatic quantum circuit encoding of a given arbitrary quantum state. *Physical Review Research*, 6(4):043008, 2024.

Weigold, M., Barzen, J., Leymann, F., and Salm, M. Data encoding patterns for quantum computing. In *Proceedings of the 27th conference on pattern languages of programs*, pp. 1–11, 2020.

## A. Right-canonicalization by SVD

In this section, we provide a detailed explanation of the right-canonicalization procedure used in Section 4.1, in particular clarifying the meaning of absorbing the non-isometric factor into the neighboring tensor to the left.

Consider a three-way MPS tensor at core  $k$ ,

$$A^{(k)} \in \mathbb{C}^{r_{k-1} \times d \times r_k}, \quad (11)$$

where  $r_{k-1}$  and  $r_k$  denote the left and right bond dimensions (ranks), respectively, and  $d$  is the physical dimension (with  $d = 4$  in our construction). To perform right-canonicalization, we reshape  $A^{(k)}$  into a matrix by grouping the physical index and the right bond index,

$$\mathbf{A}^{(k)} \in \mathbb{C}^{r_{k-1} \times (dr_k)}, \quad \mathbf{A}_{\alpha_{k-1}, (p_k, \alpha_k)}^{(k)} = A_{\alpha_{k-1}, p_k, \alpha_k}^{(k)}. \quad (12)$$

Then, we compute the singular value decomposition (SVD)

$$\mathbf{A}^{(k)} = W^{(k)} \Sigma^{(k)} (V^{(k)})^\dagger, \quad (13)$$

where  $W^{(k)} \in \mathbb{C}^{r_{k-1} \times r_{k-1}}$  and  $V^{(k)} \in \mathbb{C}^{(dr_k) \times r_{k-1}}$  have orthonormal columns, and  $\Sigma^{(k)}$  is a non-negative diagonal matrix of singular values. Since the columns of  $V^{(k)}$  are orthonormal, the matrix  $(V^{(k)})^\dagger \in \mathbb{C}^{r_{k-1} \times (dr_k)}$  satisfies the row-isometric condition

$$(V^{(k)})^\dagger ((V^{(k)})^\dagger)^\dagger = (V^{(k)})^\dagger V^{(k)} = I_{r_{k-1}}. \quad (14)$$

Therefore,  $(V^{(k)})^\dagger$  can be directly reshaped into a right-canonical MPS tensor at core  $k$ . The remaining factor  $W^{(k)} \Sigma^{(k)}$  is generally not isometric and hence cannot be retained at core  $k$ . Instead, this factor is multiplied into the neighboring matrix at core  $k-1$  by contracting it with the corresponding bond index:

$$\mathbf{A}^{(k-1)} \leftarrow \mathbf{A}^{(k-1)} \cdot (W^{(k)} \Sigma^{(k)}). \quad (15)$$

This operation preserves the value of the overall tensor network, since it merely redistributes factors within a local product of matrices, while ensuring that the updated matrix at core  $k$  remains right-canonical. By iterating the above steps from  $k = L$  down to  $k = 1$ , all matrices are transformed into right-canonical form. As a consequence, the norm of the global MPS depends solely on the first matrix  $\mathbf{A}^{(1)}$ , allowing the global normalization  $\|\psi\| = 1$  to be enforced by rescaling  $\mathbf{A}^{(1)}$  alone.

## B. Synthesis of unitaries into elementary quantum gates

After obtaining the local unitaries, we adopt Quantum Shannon Decomposition (QSD, [Shende et al., 2005](#)) based on the Block ZXZ-Decomposition ([Krol & Al-Ars, 2024](#)) to decompose each unitary into elementary quantum gates, such as single-qubit rotations and CNOT gates. Specifically, given an  $n$ -qubit unitary  $U \in \mathbb{C}^{2^n \times 2^n}$ , QSD expresses  $U$  recursively as a product of  $(n-1)$ -qubit unitaries and single-qubit rotations. By partitioning  $U$  with respect to a selected control qubit,  $U$  can be written in block form as

$$U = \begin{pmatrix} U_{00} & U_{01} \\ U_{10} & U_{11} \end{pmatrix}, \quad U_{ij} \in \mathbb{C}^{2^{n-1} \times 2^{n-1}}. \quad (16)$$

In the iterative QSD procedure, the same factorization is applied successively to the resulting  $(n-1)$ -qubit unitaries until reaching base cases of one- or two-qubit unitaries, which can be synthesized directly. This synthesis process is implemented in the UnitaryGate module of Qiskit ([Javadi-Abhari et al., 2024](#)), which we utilize to convert the local unitaries into quantum circuits.

## C. Introducing $R_Y$ and $R_Z$ rotations for circuit parameterization

In TNQE-unitary, the goal of the parameterized quantum circuit is to realize a family of unitaries that can be directly mapped onto quantum circuits. We therefore adopt a gate-based parameterization strategy, choosing  $R_Y(\alpha)$  and  $R_Z(\alpha)$  gates and together with entangling gates.

For a single qubit, any unitary operator  $U \in \mathbb{C}^{2 \times 2}$  can be expressed using three continuous rotation parameters, given by the Euler-angle decomposition

$$U(\gamma, \alpha, \beta) = R_X(\gamma) R_Y(\alpha) R_Z(\alpha), \quad (17)$$

where the rotation operators are defined as

$$R_\mu(\theta) = e^{-i\theta\mu/2} \quad \mu \in \{X, Y, Z\}. \quad (18)$$

Although Eq. (17) explicitly involves rotations around all three Pauli axes, the  $R_X$  rotation does not introduce additional expression. In particular, an  $X$ -axis rotation can be exactly represented using only  $Y$ - and  $Z$ -axis rotations via

$$R_X(\theta) = R_Z\left(\frac{\pi}{2}\right)R_Y(\theta)R_Z\left(-\frac{\pi}{2}\right). \quad (19)$$

This shows that the gates  $R_Y, R_Z$  is sufficient to parameterize arbitrary single-qubit unitaries in TNQE-unitary. Moreover, including  $R_X$  gate leads to a redundant parameterization without increasing the expression. In this work, we therefore restrict the single-qubit gate set to  $R_Y, R_Z$ , which provides an efficient circuit parameterization.

## D. More experimental results and details

We present more detailed confusion matrices in Figure 9 further illustrate the classification performance of different encodings. These findings indicate that the proposed TNQE methods effectively preserve essential features of the images during the encoding, leading to improved classification performance.

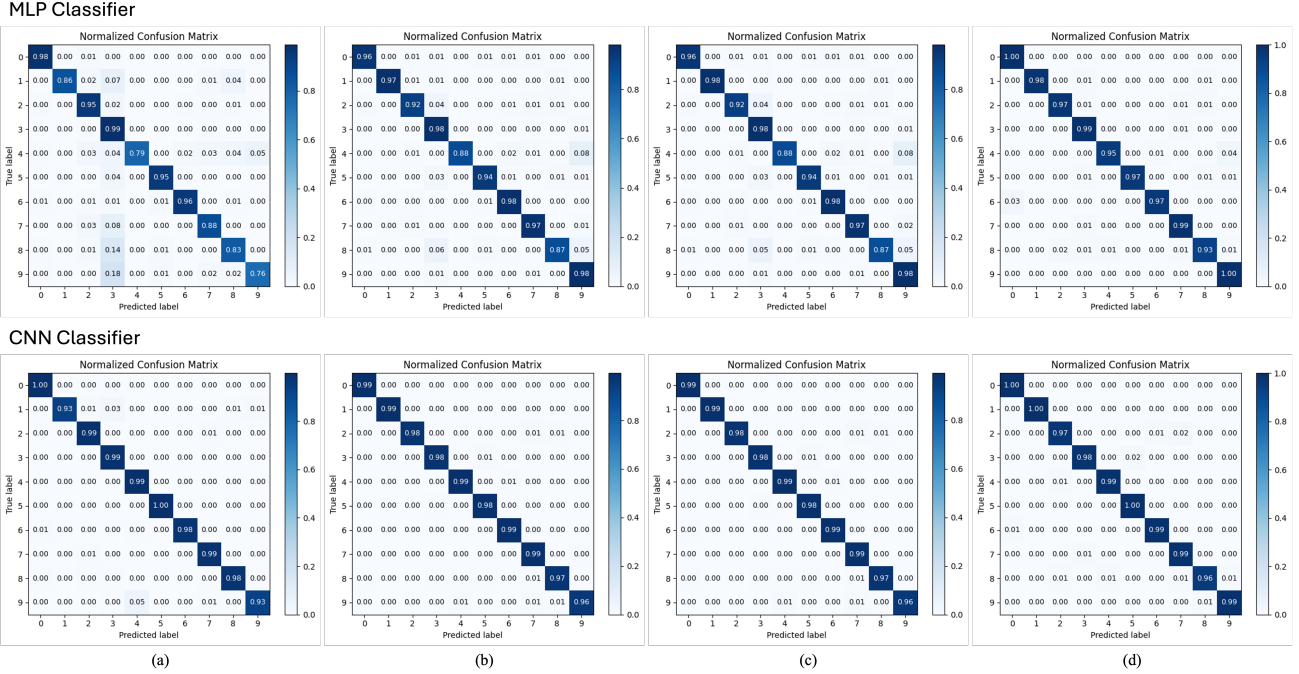


Figure 9. Confusion matrix of (a) Automatic encoding, (b) TNQE-full, (c) TNQE-core, (d) TNQE-unitary on MNIST classification task in Figure 5d using pre-trained MLP (Top) and CNN (Bottom) classifiers.

Due to page limitations in the main text, we present additional metric results in Table 6. These results closely match those in Table 4, in short, as the rank increases, the approximation quality improves, but this also leads to increased circuit complexity. Regarding the impact of number of layers in TNQE-unitary, we also present additional results in Table 7 that further confirm the observations in Figure 7, i.e., increasing the number of layers generally enhances performance. According these results, we select rank of 4 for TNQE-full and TNQE-core, and a rank of 8 for TNQE-unitary in the main text experiments. For TNQE-unitary, we choose 4 layers to achieve a good balance between performance and circuit depth.

**Details of quantum hardware.** We conduct experiments on IBM Quantum Platform, specifically using four different quantum processing units (QPUs): ibm\_torino with Heron r1: 133 qubits, 2Q error (median): 2.61E-3, 2Q error (layered):

Table 6. Ablation study on different ranks using TNQE on MNIST. The circuit structure is shown in parentheses as (qubits, depth).

Methods	Rank	1	2	3	4	5	8	9	16
Full	BCE	1.137407	0.504207	0.248129	0.125140	0.100464	0.067908	0.065382	0.093536
	PSNR	10.9041	12.9945	15.5608	19.0217	21.5318	29.9344	33.4708	34.0668
	SSIM	0.287041	0.583822	0.780099	0.906428	0.946004	0.989724	0.993186	0.969076
	Structure	(10, 7)	(11, 195)	(12, 945)	(12, 945)	(13, 4185)	(13, 4185)	(14, 17625)	(14, 17625)
Core	BCE	1.150839	0.496339	0.249040	0.124900	0.100473	0.068111	0.065349	0.092729
	PSNR	10.8891	12.9989	15.5508	19.0257	21.5332	29.8655	33.2292	33.9262
	SSIM	0.283047	0.583711	0.779720	0.906446	0.945979	0.989542	0.993234	0.969857
	Structure	(10, 4)	(18, 24)	(26, 116)	(26, 116)	(31, 242)	(34, 496)	(39, 1006)	(42, 2028)
Unitary	BCE	0.583105	0.197783	0.113675	0.113823	0.092351	0.092333	0.083594	0.083581
	PSNR	8.2066	13.7810	18.0264	18.0345	20.6001	20.5837	21.9041	21.8522
	SSIM	0.184680	0.673837	0.855882	0.855416	0.915680	0.91590331	0.938823	0.939511
	Structure	(10, 8)	(11, 56)	(12, 61)	(12, 61)	(13, 81)	(13, 81)	(14, 82)	(14, 82)

Table 7. The impact of number of layers in TNQE-unitary on image approximation quality.

Layers	1	2	3	4	5	6	8	10	12	14	16	18	20
MSE	0.045022	0.021625	0.015167	0.011249	0.008361	0.006421	0.003857	0.002621	0.001746	0.001147	0.000838	0.000652	0.000504
BCE	0.202573	0.123985	0.103954	0.092333	0.083855	0.077791	0.069254	0.064738	0.061277	0.058689	0.057237	0.056265	0.055501
PSNR	13.6188	17.2647	19.1014	20.5837	21.8803	23.1861	25.7583	27.8214	30.1595	32.8591	34.9306	37.0738	38.8589
SSIM	0.694205	0.840451	0.885914	0.915903	0.938019	0.952568	0.971858	0.981073	0.987587	0.992111	0.994204	0.995560	0.996577
Depth	21	41	61	81	101	121	161	201	241	281	321	361	401

8.81E-3; ibm\_fez with Heron r2: 156 qubits, 2Q error (median): 2.57E-3, 2Q error (layered): 4.97E-3; ibm\_kawasaki with Heron r2: 156 qubits, 2Q error (median): 1.37E-3, 2Q error (layered): 6.60E-3; ibm\_boston with Heron r3: 156 qubits, 2Q error (median): 1.26E-3, 2Q error (layered): 2.03E-3. Owing to the high cost associated with IBM quantum services, we restrict the evaluation to the first 100 samples from the test dataset in Table 5. Each each samples, we execute 50000 shots to estimate the output distribution. Nevertheless, a clear performance gap is observed, with our method significantly outperforming both amplitude encoding and automatic encoding, as also illustrated in Figure 8.

**Implementation details of quantized tensor train optimization.** Regarding the classical optimization of QTT in TNQE-full and TNQE-core, we employ the Adam optimizer (Kingma, 2014) with a learning rate of 0.01, and train for 2000 epochs on MSE loss. Regarding TNQE-unitary, we adopt more advanced optimization techniques to enhance convergence and stability. Specifically, we utilize the AdamW optimizer with a maximum learning rate of 0.03 and a weight decay of  $10^{-4}$ , combined with a one-cycle learning rate schedule for stable training, and train for 1000 epochs on KL divergence loss.

## E. Additional Discussion

**Relation to feature-based quantum-classical hybrid pipelines.** Several hybrid approaches first use classical models (e.g., CNNs) to extract low-dimensional features and then encode them into a simple quantum circuit for subsequent processing (Ranga et al., 2024; Lu & Shi, 2025). As discussed in the main text, although such hybrid approaches can in principle handle arbitrary classical data, they rely on pre-trained classical models to extract task-specific feature representations. Recovering the original input typically requires an additional classical decoder, which limits their applicability in truly end-to-end quantum machine learning settings. Moreover, once high-dimensional data are compressed into low-dimensional features, simple classical algorithms often achieve performance that substantially surpasses current quantum methods, thereby weakening the necessity of quantum processing in these pipelines. As a result, these approaches tend to exhibit advantages only for specific tasks and datasets, rather than providing a general framework for quantum machine learning.

TNQE targets a fundamentally different goal. Rather than learning specific task-features, we focus on quantum state preparation from high-dimensional inputs under realistic circuit constraints. Although tensor network decompositions can be interpreted as a form of compression, they differ fundamentally from CNN-style representation learning: QTT relies on deterministic reshaping (quantization) followed by low-rank factorization that captures multi-scale correlations, without being trained to extract high-level semantic features.

Importantly, the quantum circuits produced by TNQE admit approximate reconstruction of the original input through

measurements and simple post-processing (e.g., normalization, factorization). This property is generally absent in CNN-based hybrid approaches, where the encoding is not designed to preserve sufficient information for input-level reconstruction.

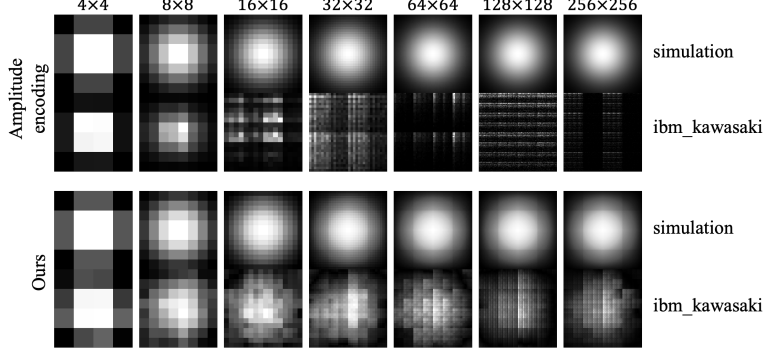


Figure 10. Comparison of simulated and real quantum results on ibm\_kawasaki with Heron r2.

**Hardware results and high-resolution stress test.** We include real quantum experiments to evaluate practical feasibility and to expose how different encoders behave under hardware noise. To this end, we create a synthetic images consisting of Gaussian ‘‘blobs’’ of varying sizes, and encode them using both amplitude encoding and TNQE-core with  $r = 4$ . We then execute the resulting circuits on ‘‘ibm\_kawasaki’’ with Heron r2 and compare the measurement outcomes, as shown in Figure 10. Both amplitude encoding and TNQE reproduce the target in simulation, whereas quantum hardware outputs degrade substantially as resolution increases. Specifically, amplitude encoding performs an exact encoding of values over the entire pixel space and, at the cost of deep circuits, can achieve very high fidelity in noiseless settings. As shown in Figure 6, its simulated results are almost indistinguishable from the ground truth. TNQE follows a similar objective: in simulation, it enables efficient encoding of high-resolution inputs, and can even represent  $256 \times 256$  color images, as demonstrated in Figure 1. However, we observe a pronounced gap between simulation and executions on real quantum hardware, which can render some encoding strategies ineffective. This discrepancy is primarily due to hardware noise, which becomes increasingly severe as circuit depth and the number of qubits grow, leading to the accumulation of errors. In practice, amplitude encoding already fails on real hardware for only  $16 \times 16$  images. While TNQE also exhibits noticeable degradation under hardware noise, it retains nontrivial structural information: even at resolutions as high as  $256 \times 256$ , the approximated results still preserve coarse blob-like contours. These observations suggest that, although current hardware noise remains a major bottleneck, TNQE shows promising potential and merits further investigation in the future works.

Importantly, in this work we do not explicitly optimize for execution on noisy quantum hardware. Our primary goal is to develop a new quantum data encoding paradigm that enables the construction of structured and circuit-efficient quantum circuits. Nevertheless, despite the absence of any noise-aware training or hardware-specific optimization, the performance of TNQE on real quantum devices already exhibits encouraging potential. This observation suggests that integrating TNQE with noise-aware optimization strategies, error mitigation techniques, and hardware-adaptive compilation in future work could further enhance its performance on real quantum hardware. Such extensions are natural and well aligned with the design of the proposed framework. Moreover, many existing approaches remain largely at the level of theoretical analysis or simulation. For example, QPIE (Brunet et al., 2024) encodes a  $256 \times 256$  image requires at least 131070 quantum operators, while BRQI, GQIR, and NEQR methods (Lisnichenko & Protasov, 2023) require 784866, 392236, and 392281 circuit depth, respectively. These resource requirements place such methods far beyond the capabilities of quantum devices (Brunet et al., 2024). Our work takes a concrete step in this direction by explicitly constructing shallower executable circuits.

**Limitations and future directions.** While TNQE demonstrates strong empirical performance and practical scalability, several open questions remain. First, the unitary-aware optimization in TNQE-unitary is primarily designed to ensure circuit realizability and explicit resource control. A more complete theoretical characterization of its optimization landscape, convergence behavior, and stability would further strengthen the understanding of when and why such parameterizations are effective, and is left to future work. Second, the performance of TNQE depends on the quality of the underlying tensor network decomposition. Continued progress in tensor decomposition algorithms, adaptive rank selection, and low-rank representations is therefore expected to translate directly into improved encoding fidelity within the TNQE framework.